Noncontact optical imaging in mice with full angular coverage and automatic surface extraction

Heiko Meyer,[1],* Anikitos Garofalakis,[1] Giannis Zacharakis,[1] Stylianos Psycharakis,[1] Clio Mamalaki,[2] Dimitris Kioussis,[3] Eleftherios N. Economou,[1] Vasilis Ntziachristos,[4] and Jorge Ripoll[1]

[1]Institute of Electronic Structure and Laser, Foundation for Research and Technology-Hellas, P.O. Box 1527, 71110 Heraklion Crete, Greece
[2]Institute of Molecular Biology and Biotechnology, Foundation for Research and Technology-Hellas, Heraklion Crete, Greece
[3]Division of Molecular Immunology, National Institute for Medical Research, The Ridgeway, Mill Hill, London NW7 1AA, UK
[4]Laboratory for Bio-Optics and Molecular Imaging, Center for Molecular Imaging Research, Massachusetts General Hospital, Harvard Medical School, Charlestown, Massachusetts 02129, USA

*Corresponding author: heimeyer@iesl.forth.gr

During the past decade, optical imaging combined with tomographic approaches has proved its potential in offering quantitative three-dimensional spatial maps of chromophore or fluorophore concentration *in vivo*. Due to its direct application in biology and biomedicine, diffuse optical tomography (DOT) and its fluorescence counterpart, fluorescence molecular tomography (FMT), have benefited from an increase in devoted research and new experimental and theoretical developments, giving rise to a new imaging modality. The most recent advances in FMT and DOT are based on the capability of collecting large data sets by using CCDs as detectors, and on the ability to include multiple projections through recently developed noncontact approaches. For these to be implemented, we have developed an imaging setup that enables three-dimensional imaging of arbitrary shapes in fluorescence or absorption mode that is appropriate for small animal imaging. This is achieved by implementing a noncontact approach both for sources and detectors and coregistering surface geometry measurements using the same CCD camera. A thresholded shadowgrammetry approach is applied to the geometry measurements to retrieve the surface mesh. We present the evaluation of the system and method in recovering three-dimensional surfaces from phantom data and live mice. The approach is used to map the measured *in vivo* fluorescence data onto the tissue surface by making use of the free-space propagation equations, as well as to reconstruct fluorescence concentrations inside highly scattering tissuelike phantom samples. Finally, the potential use of this setup for *in vivo* small animal imaging and its impact on biomedical research is discussed.   © 2007 Optical Society of America

OCIS codes: 170.3880, 040.1520, 100.3010, 110.0110.

1. Introduction

Even though optical imaging has always been the main tool used by biologists throughout the centuries, it has been relegated to imaging transparent samples and thus basically to microscopy studies. Triggered mainly by the discovery and improvement of the green fluorescent protein (GFP) [1] (see also Tsien, for a review [2]) new sources of optical contrast have appeared, functioning as reporters of gene expression and cell tracking among other applications, and enabling dynamic studies of biological processes. Even though initially only microscopy benefited from these advances, we have recently witnessed how fluorescent and bioluminescent probes are being used in whole animal imaging [3–7].

Whenever working with fluorescent or bioluminescent probes as a source of contrast, the most common approach is the use of simple photographic methods

to record planar images. These are inexpensive and have a high throughput, but do not give quantitative results or depth information [8]. On the other hand, applying tomographic approaches to similar setups does retrieve depth and give quantitative results based on the correct modeling of light propagation inside tissue [9–12]. These optical tomography approaches are mainly termed diffuse optical tomography (DOT) when using absorption and scattering as the source of contrast and fluorescence molecular tomography (FMT) when exploiting the fluorescence emission from probes or proteins.

To obtain the maximum resolution from FMT and DOT setups, large measurement data sets [13–15] and full 360° angular measurements [16] are fundamental. Thus, the ideal tomographic configuration for collecting light that has propagated through tissue would be to have sources and detectors close to but not in contact with the scattering medium, allowing straightforward acquisition, with the use of CCD cameras, of a large number of measurements and tomographic projections. In addition to offering simple experimental setups, this would enable measurement of specimens of different shapes and sizes. Such systems and corresponding techniques have recently materialized, triggered by theoretical developments in modeling arbitrarily diffuse boundaries and subsequent propagation of light in free space [17,18]. Noncontact optical tomography for one single projection has been recently verified by means of fluorescence measurements with phantoms and controlled experiments on mice [19]. In this case, a photogrammetric 3D camera was used to obtain the surface information. Data showing the capability of a setup for optical projection tomography [20,21] (OPT) to reconstruct the surface of a fixed developing limb by measuring its shadows from several projections has been presented. However, this setup has only been used to image and reconstruct organs, not whole animals. A different approach to acquire the three-dimensional (3D) surface information is used by Xenogen in their IVIS Imaging System 200 Series and following imaging systems [22]. In their apparatus, the surface topography is created by imaging the response of a structured light pattern projected onto the specimen using a scanning laser galvanometer. The surface then can be reconstructed using the phase-shift information of the parallel lines of the pattern.

To take full advantage of the noncontact approach, we have developed a full 360° tomographer for 3D *in vivo* imaging of fluorescent proteins and probes in whole animals. This novel imager offers imaging capabilities nonexisting at the moment in the field of *in vivo* imaging of fluorescent proteins and fluorophores. Using a thresholded shadowgrammetry approach for the surface acquisition, this setup is capable of reconstructing the 3D surface by measuring the projected shadow at several angles exploiting the full 360° rotation capability of the imager [23–26]. We would like to stress, however, that this approach is not capable of retrieving convex-shaped areas

where changes in the projected shadow cannot be measured. Fortunately, taking into account the surface resolution needed for optical tomography (~1 mm), most of the areas of interest in the model organism described here are nonconvex, namely, the skull (excluding the ears), the abdominal area, and extremities.

The reconstruction of the 3D surface enables the correct modeling of light propagation inside the volume defined by this surface. Additionally, the setup is capable of completing a full rotation of the specimen for each fixed source position. Measurements on cylindrical high-scattering phantom media were made, and we show reconstruction of the shape of the phantom as well as rendered reconstructed fluorescence concentration in the cylinder. The capacity of the system to quantify fluorescence signal from tubes containing different fluorophore concentrations inside cylindrical scattering media is also demonstrated. Finally we show *in vivo* results from transgenic mice that express GFP in their T cells. We targeted the thymus of the mice, and we observed the difference in signal, emerging from the front of the thoracic body area around the targeted organ, between a GFP and a nontransgenic mouse.

This paper is structured as follows. In Section 2, a detailed description of the experimental setup is given, together with the materials and the methods used. In Section 3, we describe how the 3D geometry is obtained from angularly resolved shadow projection and present studies of the positional accuracy. In Section 4, we present 3D reconstructions of fluorescence activity in a cylindrical phantom together with a quantification study for several fluorophore concentrations. In Section 5, we present preliminary *in vivo* results where the surface information is used to map the fluorescence data measured by a CCD onto the surface, by means of the free-space propagation equations. Finally in Section 6, we present a discussion on the results with our conclusions and future work.

2. Experimental Setup

To identify the different components of the optical tomography setup, 3D and 2D schematic representations of the experimental setup are shown in Fig. 1. The setup consists of a cw argon ion laser (i) (LaserPhysics, Reliant 1000 m, West Jordan, Utah 84088, USA), operating in multiline mode (emission from 457 to 514 nm). The output power can be varied from 65 to 780 mW with a fluctuation of ±0.3% over time after warm-up. The experiments were carried out inside a custom-made aluminum black anodized imaging chamber for ambient light isolation of the device (ii) (shown transparent in Fig. 1 for illustration purposes), containing an *X–Y* translation stage (iii) (model 8MT167-100) and a rotation stage (v) (model 8MR180) (both from Standa, Vilnius, Lithuania). The acquisition was performed with a 16 bit CCD camera (vi) (ANDOR Corporation, DV 434, Belfast, Northern Ireland) cooled thermoelectrically down to −70 °C for reduced dark and readout noise, with a chip size of 1024 × 1024 pixels and a

Fig. 1. System setup for 3D *in vivo* small animal imaging with all the main components numbered: i, cw Ar+ laser; ii, imaging chamber shown here transparent for illustration purposes; iii, *x–y* translation stage with fiber, collimation optics, and laser line filters; iv, custom-made diffuse light source for back illumination; v, rotation stage with custom made specimen holder (see inset: part a mounted on the stage, specimen is mounted on part b, which then is clipped into part a); vi, CCD camera; vii, SIGMA 50 mm *f*/2.8 objective; viii and ix, multimode fiber with mount; x, rail for rotation stage; xi, Isoflurane vaporizer; xii, custom-made chamber for deduction; xiii, camera power supply.

50 mm *f*/2.8 Macro objective lens vii. (Sigma, Tokyo, Japan). The system allows scanning in the *x–y* plane and rotation of the target around its *y* axis for complete angular projection acquisitions. The entire experimental procedure was computer controlled through a 3.0 GHz PC with 512 MB RAM and custom software developed under the LABVIEW environment.

The laser beam was coupled into a 600 μm UV-enhanced acrylate/nylon (UVAN) multimode fiber, (NA = 0.22, length 1.5 m, attenuation 10 dB/km, equipped with commercially available FC/PC connectors) (FiberTech GmbH, 12459, Berlin, Germany), using an antireflection-coated aspherical lens (focal length 12 mm) and an *x–y* stage (ix). The output of the fiber was then coupled into a custom fiber collimator through a similar *x–y* stage to obtain a 2 mm diameter beam on the target. The whole system was mounted on the *x–y* translation system (iii), which allowed scanning of the sources on the surface of the target. The resolution of the translation stages was 1 μm at a travel range of 100 mm and a maximum speed of 5 mm/s. The resolution of the rotation stage was 0.6 arc min (0.01°) at a maximum speed of 12°/s and a 360° continuous rotation. The translation stages with the beam expander for the scan may be either mounted next to the camera or in the optical axis of the camera, thus providing the ability to per-

form tomographic measurements in both reflection and transmission geometries. The rotation stage was fixed in an upside down position on a carrier plate (see Fig. 1), which can be moved on a rail (x) along the optical axis of the camera.

For the acquisition of the fluorescence and excitation signals, two antireflection-coated emission filters were used: a 55 mm diameter bandpass filter for GFP emission (540 nm center wavelength ±20 nm) and a 55 mm diameter bandpass filter for the excitation source (480 nm center wavelength ±30 nm) (both from Chroma Technology Corporation, Bellows Falls, Vermont, USA), both having a clear aperture of 51 mm. The above-described filters were used in the experiments explained in Sections 4 and 5. The holder for the sample consisted mainly of two parts, one of which was mounted permanently on the rotation stage, while the second one could be removed to place the sample. It is based on a simple clip system that provides good reliability and reproducibility along with quick placement of the sample (see depiction in Fig. 1).

An Isoflurane veterinary vaporizer (Tec-3, LUMIC International, Baltimore, Maryland, USA) was used to anesthetize the mice during the *in vivo* measurements. The output of the vaporizer could be directed either into the imaging chamber to a mask on the

rotation stage for maintaining anesthesia throughout the measurements or into a separate chamber (see xi in Fig. 1). To prepare the mice for the experiment, a gaseous mixture of 2% Isoflurane–3.5 l/min of oxygen was injected into the chamber where the mouse was left for 5 min before fixing it on the custom-made holder to be placed on the rotation stage. This procedure lasted less than 30 s. To keep the mouse under anesthesia during the measurements, a 1.7% Isoflurane–2.5 l/min oxygen mixture was used. The percentage of Isoflurane was varied due to age and weight of the subject and was controlled until normal breathing frequency was acquired in order to minimize movement due to muscle contraction.

We would also like to point out that in addition to the use of a scanning source device as shown in this work (see Fig. 1), appropriately collimated or focused photon beams could be correspondingly rotated or scanned in noncontact ways as well and impinge on the object from different angles. Additionally, certain illumination patterns could be projected on the animal surface rather than single point sources. It is important to note that since the presented experimental setup allows significantly large data sets to be obtained, fast inversion schemes become crucial in the efficient implementation [15,27,28] when 3D tomographic images are needed.

3. Surface Geometry Extraction and Fluorescence Molecular Tomography Data Acquisition

A series of shadow and white-light images of the subject in each rotation angle was acquired in order to reconstruct the 3D surface. This was realized using a custom 25 cm × 25 cm illuminating source (see iv in Fig. 1) that projects a homogeneous illumination pattern onto the target, which was composed of four rectangular arranged arrays of white LEDs (5 mm $\varnothing$, 50° emission angle) being diffuse reflected from a 2 mm Teflon plate on a flat 5 mm thick highly scattering white sheet of poly(methyl methacrylate) mounted in 5 cm distance to the Teflon reflector. The illumination source–target distance was ~20 cm. For the 3D surface measurement, 71 rotational steps with an increment of 5° and an integration time of

50 ms for each projection were required for a 3D map of the subject reliable enough to perform optical tomography. Because this technique deals with diffuse light, variations of the order of the mean free path (which is typically of the order of ~1 mm), do not have an impact on the reconstructed image. This means that while the surface may change during the surface acquisition due to breathing, an average surface is retrieved, which is accurate enough for FMT or DOT. The integration time for each projection was 50 ms.

A. Surface Reconstruction Algorithm

The surface information was obtained using the simple approach of adding all the projections (shadows) of the specimen, equivalent to the radon transform method [29] with a constant filter. Before doing so, each image I for each projection angle θ_i was thresholded, converting it into a binary image $\bar{I}$,

$$\bar{I}(x, y, \theta_i) = \begin{cases} 1 & \forall I(x, y, \theta_i) > I_{th}^{(i)} \\ 0 & \forall I(x, y, \theta_i) \leq I_{th}^{(i)}, \end{cases} \quad (1)$$

where x and y correspond to the pixels in the x and y directions, respectively, and I_{th} is the threshold value, which we set to 50% of the maximum value of the image, i.e., $I_{th}^{(i)} = 0.5 \times \max\{I(x, y, \theta_i)\}$, which we found to be the most robust approach for several signal-to-noise cases, ensuring proportional application of the thresholds to the existing illumination intensity, instead of using, for example, a fixed number of counts. Results for the geometry extraction algorithm are shown in Figs. 2b and 2c, where we present the raw and the thresholded data, respectively, for a single projection. The test subject was a plastic toy witch, which is shown in Fig. 2a where a white-light image for the same projection is presented.

Once all images have been thresholded, the axis of rotation has to be determined. One way of finding the position of the axis of rotation when dealing with the radon transform is to find where the variance in the reconstructed image is maximum [30] versus the center of rotation. This technique, however, does not yield good results when dealing with binary im-
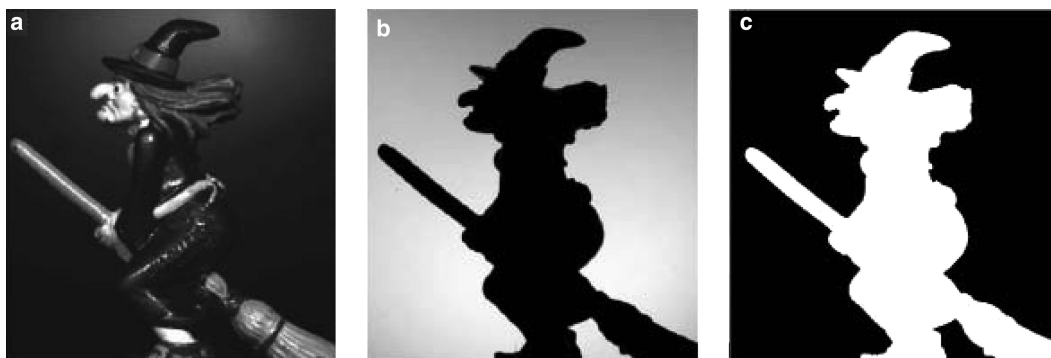

Fig. 2. a, Shadow image as acquired from the system; b, shadow image thresholded to 50% of maximum intensity; c, homogeneous white-light image for the same projection.
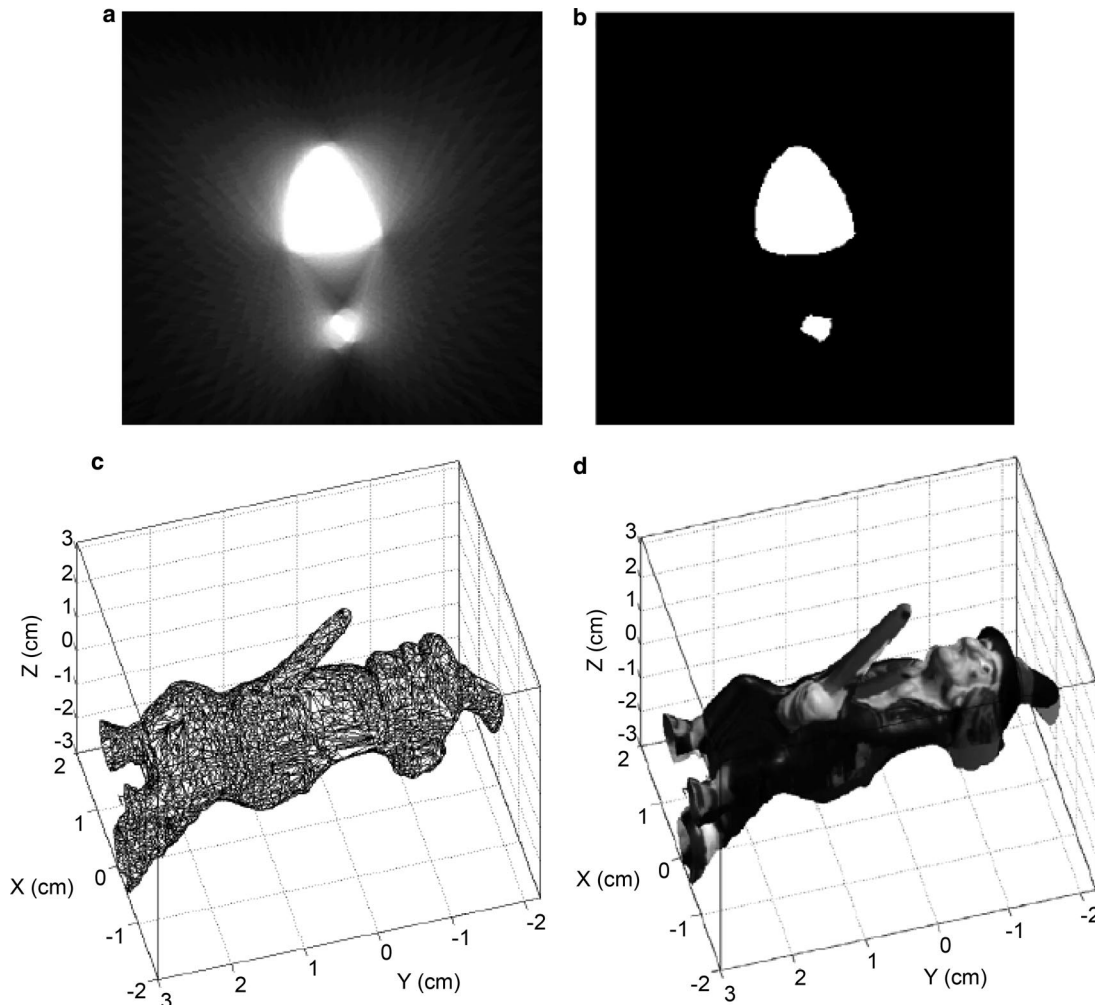
Fig. 3. a, Backprojected data for one slice (each slice corresponds to one pixel line of the CCD) obtained with 72 projections; b, thresholded data; c, reconstructed surface mesh; d, rendered reconstruction.

ages as in our case, and especially with specimens subject to small changes in position due to breathing, for example. We have found that the most reliable approach for finding the position of the axis of rotation is to determine the position as the one that minimizes the error between each projection and its mirrored 180° counterpart, using the following formula:

$$x_{center}^{(i)} = \min\left\{ \left| \bar{I}(x - x_{center}^{(i)},\ y,\ \theta_i) \right. \right.$$
$$\left. \left. - \bar{I}(-(x - x_{center}^{(i)}),\ y,\ \theta_i + \pi) \right| \right\}. \quad (2)$$

Equation (2) is used for each $(\theta_i,\ \theta_i + \pi)$ pair, and the final axial position is found as the average. We emphasize that Eq. (2) has proven to be very useful *in vivo* where slight changes in position over time are observed. Once the axis of rotation has been determined, each angular projection is added up, forming the 3D volume. Once the volume occupied by the specimen is found, the surface can be easily extracted by finding those values slightly under unity (which would correspond to those pixels that appear in all projections) and using MATLAB's (The Mathworks, Inc.) edge-based isosurface extraction algorithm. We

have found that selecting the surface as the boundary of those pixel values that are over 0.8 consistently yields good results. Results for the same test case presented in Fig. 2 are shown in Figs. 3a and 3b for the raw and thresholded reconstructed slices, respectively. A coarse surface mesh is shown in Fig. 3c, for 9033 triangular mesh vertices (typical numbers of vertices used are 90,000). The final result for the case of the toy witch is shown in Fig. 3d were the surface was rendered giving each triangular mesh a gray-scale color related to the intensity obtained for a white-light image for representation purposes and in order to accurately identify anatomical landmarks, which should be compared with the image of Fig. 2a.

As we have already mentioned, one of the main drawbacks when using this type of approach is the fact that convex surfaces cannot be reconstructed. However, to our benefit, very few regions of the small animals used for imaging actually present convexity. Among them would be, for example, the regions under the fore and hind legs. When the complete (convex and concave) surface areas are needed, more advanced surface extraction approaches should be used
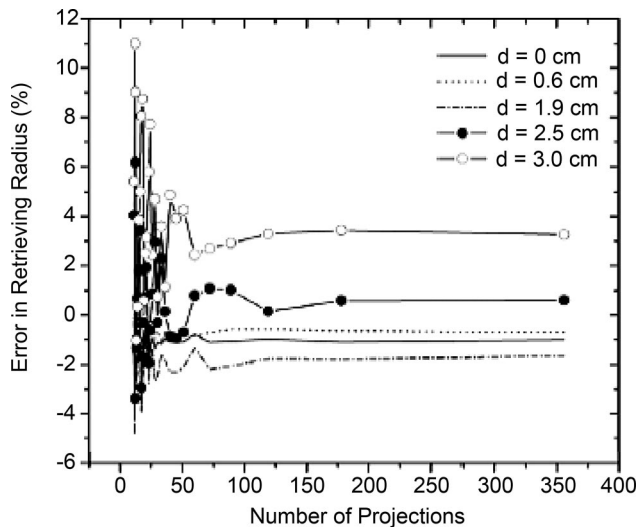
Fig. 4. Error of the reconstructed radius versus number of projections. The maximum error was found to be ±0.02 mm of the original radius from a rigid rod of 10 mm diameter.

Fig. 5. Reconstructed radius versus distance in respect to the center of rotation for various numbers of projections.

such as 3D surface cameras [18,19] or spatially modulated illumination patterns [31].

B. Surface Reconstruction Accuracy

To study the accuracy of our surface reconstruction setup, we performed experiments where we varied the position of the sample with respect to the axis of rotation and measured several different numbers of projections, varying from 360 projections to 10. In all cases, the numerical aperture of the camera was fixed to its minimum $\frac{1}{32}$ to ensure that the sample was in focus, independent of its position. A bar of 10 mm diameter and 10 cm length was mounted on a 10 mm × 10 mm positioning bar on the rotation stage in five defined distances, 0 (center of rotation), 6.15, 18.95, 24.65, and 29.9 mm, respectively, to the center of rotation. In Fig. 4, we present results for the error in retrieving the radius versus number of projections for the different bar distances presenting the error in percentage. For the cases studied here, very similar accuracy is obtained for 72 and higher number of projections, which was then used to be the minimum number of projections in order to acquire a well-defined surface. Additionally, it has to be noted that even for optimal working conditions and a phantom placed in the center of rotation, an error of 1% is present due to the pixel size. In Fig. 4, this error was established to be 0.008 cm, which is comparable with a pixel size of 0.0169 cm × 0.0169 cm. Further we would like to accentuate that the center of rotation is not known with high precision since it is difficult to maintain the rod exactly on the center of rotation along its entire axis. Hence the lowest error retrievable is determined basically by the pixel size.

Figure 5 shows a plot of the error variation with respect to the number of projections per revolution (72, 178, and 356 projections) retrieved from the measurement described above. This has been performed in order to minimize the number of measurements
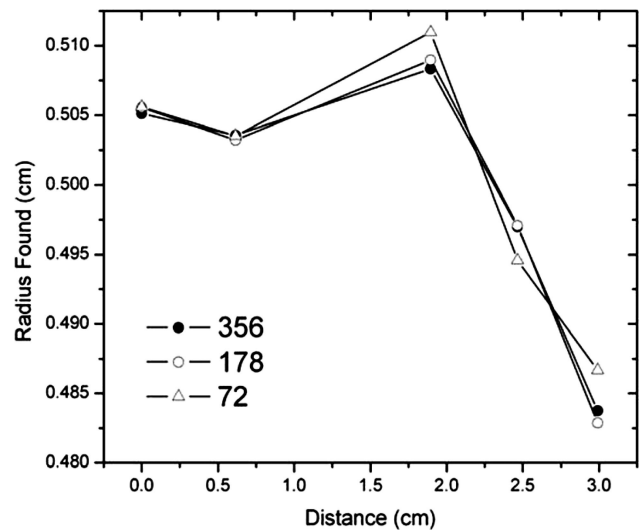
with respect to the accuracy. We have found the maximum error to be ±0.015 cm for a rigid rod of 5 mm radius being mounted 3 cm away from the center of rotation. Since the main application is for *in vivo* imaging, we expect, in this case, to measure an average of the surface of the mouse due to breathing and movement. In this case, the reconstructed accuracy is expected to be less. However, we would like to emphasize that since the setup is used for diffuse light imaging, any change in the order of the transport mean free path (typically 1 mm) does not have a measurable impact on the reconstructed data. We therefore believe that the accuracy of this approach is appropriate for *in vivo* imaging.

Additionally, and as expected, the retrieved accuracy degrades as the object is placed further away from the center of rotation. To understand this better, in Fig. 5, we plot the retrieved radius versus distance from the rotation axis. As can be seen from this figure, the error in retrieving the radius is practically constant up to a distance of 2 cm from the center of rotation. From then on, there is a linear decay. Since typical distances when measuring mice usually do not surpass 2 cm, the proposed surface extraction setup will yield good results. However, it is expected that in cases in which the specimen is significantly larger, the retrieved surface values located further away will suffer from distortions due mainly to the effect of perspective (i.e., objects are measured smaller as they are located further away from the camera). For this reason, prior to the measurements presented in Figs. 4 and 5, we had measured the effect of perspective on the data, finding that the changes in size for typical mouse distances were of the order of 0.017 cm, and hence within the expected error found. Since in an ideal case the resolution of the recovered surface should be dependent only on the image of the actual pixel size of the CCD camera in the plane in focus, we believe that the contribution of the effect of perspective to the error is important.

In those cases where higher surface resolution is needed, a scheme, which accounts for perspective is necessary.

C. Fluorescence Molecular Tomography Data Acquisition

Initially, the subject had to be placed and fixed on the rotation stage and the system properly aligned to the center of rotation. After that, the number and arrangement of sources was chosen and set through the LABVIEW software along with the number of projections (rotation steps), according to the size and shape of the subject. The source configuration was chosen, so that for all projections, the beam for each source position impacts onto the target area. Then the fluorescence and excitation signals were acquired with the corresponding filters. One image was recorded for each source position and rotation angle resulting in an $N_x \times N_y \times N_s \times N_r$ array of images, where N_x and N_y are the number of pixels in x and y (in our measurements 512×512 after a 2×2 binning), N_s is the number of sources, and N_r is the number of projections. The positions of the sources were also imaged on a white highly scattering Teflon sheet, placed at the plane in focus of the camera, in order to accurately calculate the center position of each source and the pixel dimensions in centimeters.

Two types of data are presented in this work, phantom data and *in vivo* data. All data were taken in reflection mode. We present the phantom data as a means of calibrating our setup, presenting a 3D image reconstruction of a fluorescent tube, and studying the linear dependence of concentration versus FMT reconstruction. The *in vivo* measurements are presented as raw fluorescence data projected by means of the free-space equations onto the 3D surface. A thorough study of the validation of the *in vivo* 3D reconstructions will be presented in a future paper. For the *in vivo* measurements, we have used transgenic mice expressing GFP under control of CD2 promoter in all T cells (CD2-GFP), which were generated as described previously [32]. The mice were backcrossed for at least ten generations in the C57B1/10 (B10) genetic background. All mice were bred in the Institute of Molecular Biology and Biotechnology animal facility under barrier conditions in accordance with established guidelines. The experiments were carried out with 4- to 6-week-old male CD2-GFP transgenic and B10 control mice.

Due to the black fur of B10 mice, the preparation of the subjects for the experiment included also shaving the hair to expose the skin at the region of interest. During the procedure, the mouse was anesthetized using Avertin, the dose depending on the subject's body weight and age ($\sim$16.1 μl/g for adult mice). The injection was given intraperitonially resulting in a time window of 40 min, enough for the procedure to be completed. The experiment was carried out after 24 h to minimize a possible interaction between Avertin and Isoflurane. Our main concern in this work is to show the accuracy of the surface acquisition method and how it can be implemented for *in vivo* imaging.

D. Fluorescence Molecular Tomography Data Reconstruction

The FMT data reconstruction was performed by inverting the forward model using the algebraic reconstruction technique (ART) with positive restriction [29,33]. ART is an iterative method for the reconstruction of a two-dimensional image from one-dimensional input data, used in computed tomography scanning. It is based on the assumption that the cross section of a tomographic image consists of an array of unknowns in terms of measured projection data. As an iterative method, it follows a procedure, which first starts with an assumed initial image function for each pixel of the reconstructed image. The projection data through the reconstructed image are calculated for one certain angle and are then compared with the measured projection data. During each iteration, the image function is modified in order to reduce the difference between the reconstructed and measured data. This procedure is repeated for various iterations (in our case for 400) until the difference between the calculated and the measured projections are negligible. For the reconstruction of the phantom and the *in vivo* data achieved from the measurements described in Sections 4 and 5, the initial guess for the local fluorophore concentration was estimated to be zero.

4. Phantom Results

As mentioned in Section 3, we studied phantom data as a means of calibrating our setup. To that end, experiments were performed on a hollow 20 mm Teflon cylinder with a wall thickness of 0.5 mm filled with an agarous solution with a scattering coefficient $\mu_s' = 15$ cm^{-1} and an absorption coefficient $\mu_\alpha = 1.4$ cm^{-1} in order to test the quality of the reconstructed surface and its impact in the 3D reconstruction of fluorophore concentration. Quantification measurements have been performed using borosilicate microcapillary tubes of 1.6 mm outer and 1.2 mm inner diameter containing different carboxyfluorescein succinimidyl ester (CFSE) concentrations (1, 50, and 100 μmol) embedded in the phantom at a center-to-center distance from the capillary to the cylinder of 5 mm. The total number of projections were 4 at 0°, 10°, 20°, and 30° with respect to the incident sample position where the tube is in the closest position to the camera, for a source grid of 3×3 sources spanning from -8.5 to 8.5 mm in the x direction and -5.9 to 5.9 mm in the y direction with respect to the center of the image. For the detection area, we used an 18×12 detector grid covering an area of 2.006 cm^2, with a detector size of 1 mm^2. The detector size is determined as follows: the true pixel size on the in-focus sample is calculated from the known center-to-center distance of two sources and the physical pixel size of the CCD chip. The pixels, which represent an area of 1 mm $\times$ 1 mm in the focal plane are then defined as one single detector.

The reconstructions were obtained by using the free-space equations [17] and the Kirchhoff approxi-

mation [28,34], normalizing the fluorescence data by the excitation data following the approach of Ntziachristos *et al.* [33]. The transformation from the CCD measurements onto the surface is the inverse of what is proposed in Ref. [17] where the free-space propagation formula is presented to relate the outward flux measured at the interface to the measurement at the CCD. In the case presented here, the outward flux at any point of the surface visible to the CCD camera is related to the actual measurement at the CCD as [17,35]

$$J_{\text{det}}(r_d) = \frac{1}{\pi} \int_S J_n(r') \Gamma(r', \, r_d) \mathrm{d}S' \quad r \in S, \quad (3)$$

where we have assumed that the surface emits like a Lambertian source [36,37], and

$$\Gamma(\mathbf{R}) = I(\mathbf{R}, \, \mathbf{u}_{\mathbf{r}_c - \mathbf{R}}) \cos\theta \, \frac{\cos\theta'}{|\mathbf{r}_c - \mathbf{R}|^2} A \, dB, \quad (4)$$

where $\mathbf{r}_c$ is a vector that represents the center of the lens and $\cos\theta = \mathbf{b} \cdot \mathbf{u}_{\mathbf{r}_c - \mathbf{R}}$ and $\cos\theta' = \mathbf{m} \cdot \mathbf{u}_{\mathbf{R} - \mathbf{r}_c}$ are the cosines of the angles subtended with the dB and A, respectively. This approximation is equivalent to a fiber of aperture A and surface normal $\mathbf{m}$ located a distance $|\mathbf{r}_c - \mathbf{R}|$ from the irradiating source.

In the case where we have all of the surface measured in focus (i.e., in the case of small numerical apertures, for example), the relation of Eq. (3) becomes a linear dependence between the CCD measurements and the outward flux, where the CCD pixels have an image detector area on the surface. This detector area depends on the absolute distance between the CCD camera lens and the surface, as

$$J_{\text{det}}(r_d) = \frac{1}{\pi} J_n(\mathbf{R}, \, z) \cos\theta \, \frac{\cos\theta'}{|\mathbf{r}_c - \mathbf{R}|^2} \, dA \quad r \in S. \quad (5)$$

Note that in the more general case where Eq. (5) has contribution from areas that are out of focus, solving for J_n actually becomes a deconvolution, with the inherent difficulties that such a transformation has, such as filtering, noise gain, artifacts, etc.

The data were inverted using ART [29] for 400 iterations. Typical times for surface extraction and fluorophore reconstruction were of the order of 20 min on a 2 GHz PC with 1 GB RAM.

Results for the reconstructions are shown in Fig. 6. Figure 6a presents the 3D reconstructed surface of an agarous phantom with reconstructed fluorescence for the reflection mode. As can be seen in this figure, both the radius of the cylinder and the position of the capillary tube containing CFSE are retrieved with an accuracy of approximately 5% (please note that the center of rotation is not necessarily located at the origin). A cross section in the *x–z* plane is shown in the inset of Fig. 6b.

The results for the quantification are shown in Fig. 6b were reconstructed mean fluorescence intensity values achieved with the FMT system versus the CFSE concentration in the microcapillary tube of the agarous phantom (1, 50, and 100 µmol solved in 1× phosphate-buffered saline solution with pH of 12) are presented. As can be inferred from this figure, the FMT reconstructed values can be calibrated to reflect the actual concentration of CFSE. It must be noted that this type of calibration has to be performed for each fluorophore under study if one intends to represent the measurements in terms of fluorophore concentration. Also, even though this quantification study has been performed in a homogeneous phantom with optical properties similar to those of mice in the GFP excitation range, we would like to state that thorough studies of the effect of inhomogeneities present have been presented recently [38] proving
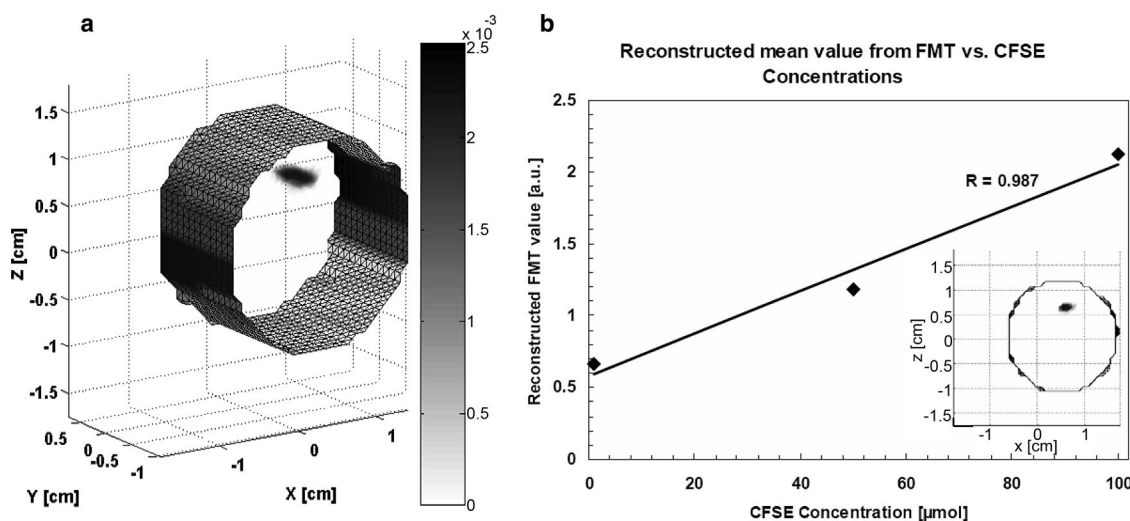

Fig. 6.   a, Three-dimensional reconstructed surface of an agarous phantom with reconstructed fluorescence using a 50 µmol concentration of CFSE in 1× phosphate-buffered solution with a pH of 12. The microcapillary was placed in a center-to-center distance of 5 ± 0.05 mm with respect to the center of the phantom, b, reconstructed mean fluorescence intensity values achieved with the FMT system versus CFSE concentration in the microcapillary tube of the agarous phantom (1, 50, and 100 µmol). (Inset shows cross section of the reconstructed fluorescence according to the values given in a.)

that the normalized approach used here [33] is extremely robust, even in highly heterogeneous media.

5. *In Vivo* Results

To present the potential that the setup has on imaging small animals, and in particular in DOT or FMT applications, we applied the methodology presented in the previous section to map the fluorescence raw data onto the 3D surface of the mouse. Using this approach, it is now feasible to render the fluorescence activity data on the surface of the mouse and have a realistic view of what would be measured in contact.

In vivo results are presented in Fig. 7, where we present the *in vivo* results of a CD2-GFP mouse (Figs.
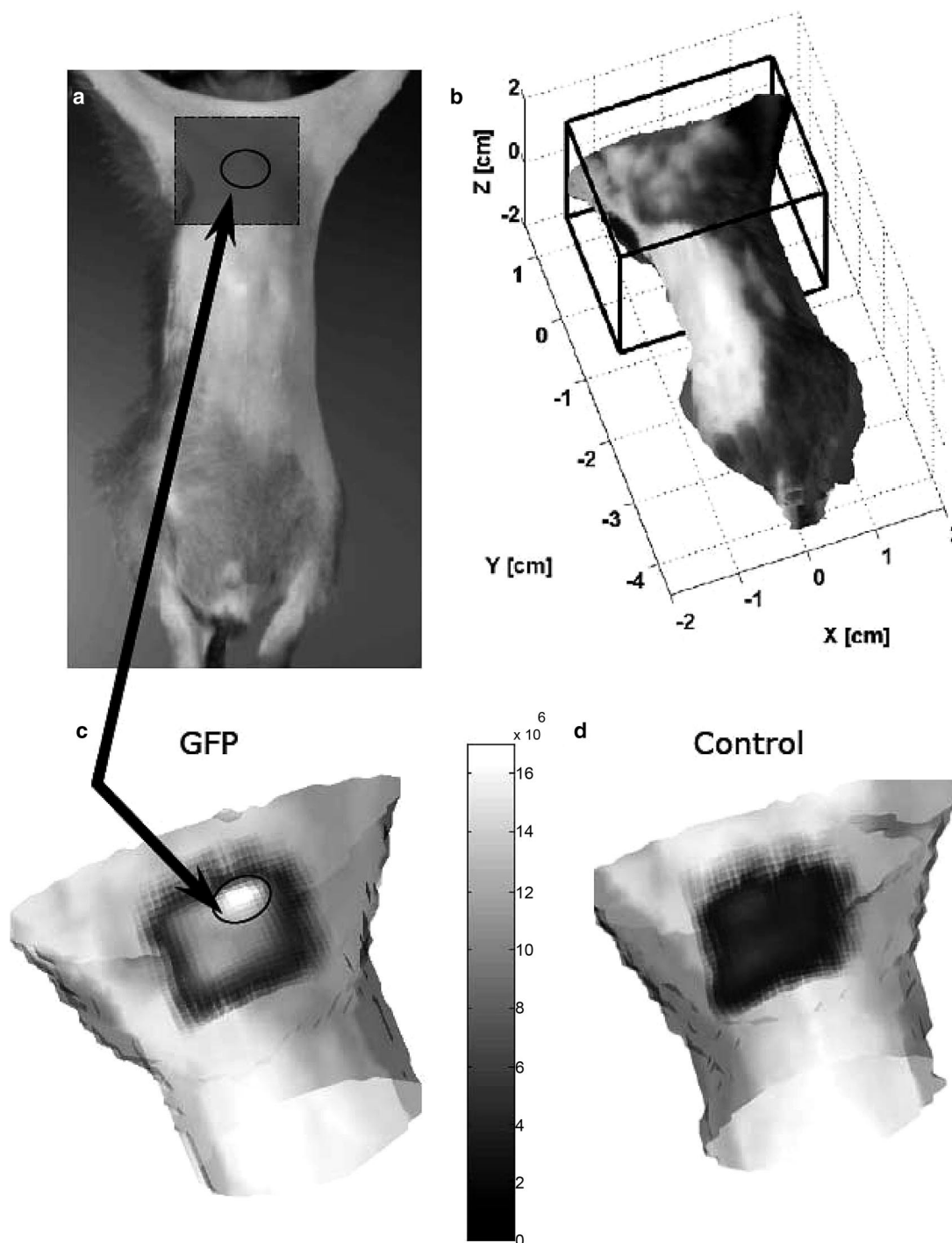
Fig. 7. *In vivo* results of a–c, a CD2-GFP mouse and d, a nontransgenic C57B1/10 mouse. The arrows indicate the position of the tumor. a, The flat image with marked detector area of 10×10 detectors, b, the rendered surface with region of interest. Presented in c, *in vivo* result of GFP expressing thymocytes in the thymus of a CD2-GFP mouse ($\sim 10^8$ cells), and d, a nontransgenic C57B1/10 control mouse. Note that the signal in the control mouse is due to autofluorescence of the skin.

7a–7c) and a nontransgenic C57B1/10 mouse as a control measurement (Fig. 7d). Figure 7a shows the flat image with a marked detector area of 10×10 detectors, while Fig. 7b gives an idea of the rendered surface with a region of interest (ROI) that corresponds to the reconstructed surface in Figs. 7c and 7d. Figure 7c reveals the *in vivo* results of GFP expressing thymocytes in the thymus of a CD2-GFP mouse ($\sim 10^8$ cells), and Fig. 7d for a nontransgenic C57B1/10 control mouse. The arrows indicate the position of the thymus. Note that the signal in the control mouse is due to autofluorescence of the skin. The total acquisition time for the data presented in Fig. 7 was ~ 45 min including the measurements for fluorescence (in this case EGFP fluorescence), excitation, surface reconstruction, and beam positions using a 4×4 source matrix for the exposure of a 10×10 mm area of observation that covered the ROI where the thymus is expected. As can be seen from Fig. 7, the thymus can be seen even without performing a tomographic reconstruction. It is expected that this organ will be feasible to be studied *in vivo* even using GFP, which lies in the region of high absorption of hemoglobin. Another fact that must be considered when imaging in the visible, is the strong presence of autofluorescence. This can be clearly seen in Fig. 7d where the control mouse exhibits a signal of approximately $2 - 3 \times 10^5$ counts in contrast to the 16×10^5 counts in the fluorescence signal, even though it is a nontransgenic mouse. This is the main factor that limits the signal-to-noise ratio when imaging in the visible and has to be accounted for if high sensitivity is required [39].

6. Conclusions

In this study, we have presented the design, implementation, and initial testing in phantoms as well as in live mice of a novel 3D imaging system suitable for *in vivo* noncontact optical tomography. The approach presented here is useful due to its simplicity and low cost. Furthermore it is highly advantageous in comparison with fiber-based systems or fixed geometry setups since it provides the ability to acquire large data sets and number of projections as well as the ability to image arbitrary shapes without the need of matching fluids or imaging chambers.

Following preliminary studies that will be presented in a future publication, we have found it to be appropriate for imaging the spleen, thymus, testes, limbs, and head, and therefore believe it will prove useful in most molecular imaging applications. The technology could also be ideal for brain studies in small animals, since no animal immersion in matching fluids or assumptions for the boundary would be required.

The system provides accurate surface reconstruction of nonconvex objects of arbitrary shapes placed in the center of rotation of the system. We have found that the resolution for the surface reconstruction is suitable for DOT and FMT measurements.

A more accurate boundary extraction could require the use of optimized photogrammetry systems or other surface extraction systems that achieve submillimeter 3D accuracy such as the approach presented here. Improvement could be achieved by the use of better illumination schemes, optimized fields of view, and more projection angles. An added complexity that may arise in *in vivo* imaging is that breathing or other movement may decrease surface description accuracy. To the advantage of the technology, however, is the fact that the optical measurements collected would generally average data from several breathing cycles of a mouse, so that a mean surface estimation is obtained. Breathing-controlled triggering is an alternative to collecting better quality data. Availability of anatomical information (shape of the surface) from the photogrammetric studies further improves the visual interpretation of the results, since reconstructed volumes can be readily coregistered with surface anatomical features.

It is important to note that since the presented experimental setup allows significantly large data sets to be obtained, fast inversion schemes become crucial in the efficient implementation [15,27,28] in 3D optical tomography. The inversion algorithm could also be further improved for faster more reliable reconstruction and rendering of the fluorescence data in 3D, thus fully exploiting the surface extraction capabilities of the system. In terms of instrumentation in the future, the setup could be improved by minimizing the time required for one full experiment by designing and automating a system for filter alteration and autofocus zoom objectives as well as an x–y positioning system for the subject to enable the observation of various areas of interest (such as *in vivo* imaging of fluorescent protein emission in single organs).

The system at the moment is being used to monitor GFP expression in T lymphocytes *in vivo* in murine models. However, noncontact imaging as described here is not limited to small animals. The utilization of noncontact technologies could facilitate more generic use of the technique with tissues of arbitrary boundaries. Therefore, the same instrument could be used for different target organs and imaging applications, although the technique today seems to be applicable only to instances where no body hair obstruct measurements. The translation of noncontact optical tomography to clinical applications is straightforward, opening new pathways of imaging disease and drug response *in vivo*.

Overall the free-space approach can offer a significantly higher level of flexibility in using optical imaging and tomography and could lead to high performance optical tomographic investigations by enabling the collection of superior information content data sets compared with contact measurement systems. Finally the setup design allows for the straightforward use of the time-resolved technology further increasing the obtained data content [16].

References

1. N. C. Shaner, R. E. Campbell, P. A. Steinbach, B. N. G. Giepmans, A. E. Palmer, and R. Y. Tsien, "Improved monomeric red, orange and yellow fluorescent proteins derived from *Discosoma sp.* red fluorescent proteins," Nat. Biotechnol. **22,** 1567–1572 (2004).

2. R. Y. Tsien, "The green fluorescent protein," Annu. Rev. Biochem. **67,** 509–544 (1998).

3. R. Weissleder and V. Ntziachristos, "Shedding light onto live molecular targets," Nat. Med. **9,** 123–128 (2003).

4. V. Ntziachristos, C. Bremer, E. E. Graves, J. Ripoll, and R. Weissleder, "*In vivo* tomographic imaging of near-infrared fluorescent probes," Molecular Imaging **1,** 82–88 (2002).

5. V. Ntziachristos, J. Ripoll, L. V. Wang, and R. Weissleder, "Looking and listening to light: the evolution of whole-body photonic imaging," Nat. Biotechnol. **23,** 313–320 (2005).

6. V. Ntziachristos, E. A. Schellenberger, J. Ripoll, D. Yessayan, E. Graves, A. Bogdanov, Jr., L. Josephson, and R. Weissleder, "Visualization of antitumor treatment by means of fluorescence molecular tomography with an annexin V-Cy5.5 conjugate," Proc. Natl. Acad. Sci. U.S.A. **101,** 12294–12299 (2004).

7. V. Ntziachristos, C. Tung, C. Bremer, and R. Weissleder, "Fluorescence molecular tomography resolves protease activity *in vivo*," Nat. Med. **8,** 757–760 (2002).

8. R. M. Hoffman, "Green fluorescent protein imaging of tumour growth, metastasis, and angiogenesis in mouse models," Lancet Oncology **3,** 546–556 (2002).

9. E. M. Hillman, J. C. Hebden, M. Schweiger, H. Dehghani, F. E. Schmidt, D. T. Delpy, and S. R. Arridge, "Time resolved optical tomography of the human forearm," Phys. Med. Biol. **46,** 1117–1130 (2001).

10. J. C. Hebden, A. Gibson, T. Austin, R. M. Yusof, N. Everdell, D. T. Delpy, S. R. Arridge, J. H. Meek, and J. S. Wyatt, "Imaging changes in blood volume and oxygenation in the newborn infant brain using three-dimensional optical tomography," Phys. Med. Biol. **49,** 1117–1130 (2004).

11. V. Ntziachristos and R. Weissleder, "Charge-coupled-based scanner for tomography of fluorescent near-infrared probes in turbid media," Med. Phys. **29,** 803–809 (2002).

12. G. Zacharakis, J. Ripoll, R. Weissleder, and V. Ntziachristos, "Fluorescent protein tomography scanner for small animal imaging," IEEE Trans. Med. Imaging **24,** 878–885 (2005).

13. J. Culver, V. Ntziachristos, M. Holboke, and A. Yodh, "Optimization of optode arrangements for diffuse optical tomography: A singular value analysis," Opt. Lett. **26,** 701–703 (2001).

14. E. E. Graves, J. P. Culver, J. Ripoll, R. Weissleder, and V. Ntziachristos, "Singular-value analysis and optimization of experimental parameters in fluorescence molecular tomography," J. Opt. Soc. Am. A **21,** 231–241 (2004).

15. V. A. Markel and J. C. Schotland, "Symmetries, inversion formulas, and image reconstruction for optical tomography," Phys. Rev. E **70,** 056616 (2004).

16. G. M. Turner, G. Zacharakis, A. Soubret, J. Ripoll, and V. Ntziachristos, "Complete-angle projection diffuse optical tomography by use of early photons," Opt. Lett. **30,** 409–411 (2005).

17. J. Ripoll, R. B. Schulz, and V. Ntziachristos, "Free-space propagation of diffuse light: theory and experiments," Phys. Rev. Lett. **91,** 103901 (2003).

18. R. B. Schulz, J. Ripoll, and V. Ntziachristos, "Noncontact optical tomography of turbid media," Opt. Lett. **28,** 1701–1703 (2003).

19. R. B. Schulz, J. Ripoll, and V. Ntziachristos, "Experimental fluorescence tomography of tissues with noncontact measurements," IEEE Trans. Med. Imaging **23,** 492–500 (2004).

20. J. Sharpe, "Optical projection tomography," Annu. Rev. Biomed. Eng. **6,** 209–228 (2004).

21. J. Sharpe, U. Ahlgren, P. Perry, B. Hill, A. Ross, J. Hecksher-Sørensen, R. Baldock, and D. Davidson, "Optical projection tomography as a tool for 3D microscopy and gene expression studies," Science **296,** 541–545 (2002).

22. XENOGEN, U.S. patent application 20060268153, (6 November 2006).

23. D. J. Lee, X. Q. Xu, J. Eifert, and P. C. Zhan, "Area and volume measurements of objects with irregluar shapes using multiple silhouettes," Opt. Eng. **45,** 027202 (2006).

24. R. T. Whitaker and V. Elangovan, "A direct approach to estimating surfaces in tomographic data," Med. Image Anal. **6,** 235–249 (2002).

25. G. Tognola, M. Parazzini, C. Svelto, P. Ravazzani, and F. Grandori, "A fast and reliable system for 3D surface acquisition and reconstruction," Image Vis. Comput. **21,** 295–305 (2003).

26. D. Rypl and P. Krysl, "Triangulation of 3D surfaces," Eng. Comput. **13,** 87–98 (1997).

27. J. Ripoll, M. Nieto-Vesperinas, R. Weissleder, and V. Ntziachristos, "Fast analytical approximation for arbitrary geometries in diffuse optical tomography," Opt. Lett. **27,** 527–529 (2002).

28. J. Ripoll and V. Ntziachristos, "Iterative boundary method for diffuse optical tomography," J. Opt. Soc. Am. A **20,** 1103–1110 (2003).

29. A. Kak and M. Slaney, *Principles of Computerized Tomographic Imaging* (IEEE, 1988).

30. J. R. Walls, J. G. Sled, J. Sharpe, and R. M. Henkelman, "Correction of artefacts in optical projection tomography," Phys. Med. Biol. **50,** 4645–4665 (2005).

31. B. W. Rice, H. Xu, and C. Kuo, "Surface construction using combined photographic and structured light information," U.S. patent application 20060268153 (4 May 2006).

32. J. de Boer, A. Williams, G. Skavdis, N. Harker, M. Coles, M. Tolaini, T. Norton, K. Williams, K. Roderick, A. Potocnik, and D. Kioussis, "Transgenic mice with hematopoeitic and lymphoid specific expression of Cre," Eur. J. Immunol. **33,** 314–325 (2003).

33. V. Ntziachristos and R. Weissleder, "Experimental three-dimensional fluorescence reconstruction of diffuse media using a normalized Born approximation," Opt. Lett. **26,** 893–895 (2001).

34. J. Ripoll, V. Ntziachristos, R. Carminati, and M. Nieto-Vesperinas, "The Kirchhoff approximation for diffusive waves," Phys. Rev. E **64,** 051917 (2001).

35. J. Ripoll and V. Ntziachristos, "Imaging scattering media from a distance: theory and applications of non-contact optical tomography," Mod. Phys. Lett. B **18,** 1403–1431 (2004).

36. A. Ishimaru, *Wave Propagation and Scattering in Random Media* (Academic, 1978), Vol. 1.

37. M. Born and E. Wolf, *Principles of Optics,* 7th ed. (Cambridge U. Press, 1999).

38. A. Soubret, J. Ripoll, and V. Ntziachristos, "Accuracy of fluorescent tomography in the presence of heterogeneities: study of the normalized Born ratio," IEEE Trans. Med. Imaging **24,** 1377–1386 (2005).

39. A. Soubret and V. Ntziachristos, "Fluorescence molecular tomography in the presence of background fluorescence," Phys. Med. Biol. **51,** 3983–4001 (2006).